Geophysical Research Letters

RESEARCH LETTER
10.1029/2025GL120000

Teleseismic Radial Anisotropy Reveals a Sill-Dominated Magma Reservoir Beneath the Valles Caldera, New Mexico

Gaoshan Guo[1], Haiqiang Lan[2], Tao Xu[3], and Qinya Liu[1,4]

[1]Department of Physics, University of Toronto, Toronto, ON, Canada, [2]State Key Laboratory of Lithospheric and Environment Coevolution, Institute of Geology and Geophysics, Chinese Academy of Sciences, Beijing, China, [3]Key Laboratory of Deep Petroleum Intelligent Exploration and Development, Institute of Geology and Geophysics, Chinese Academy of Sciences, Beijing, China, [4]Department of Earth Sciences, University of Toronto, Toronto, ON, Canada

Key Points:

- Teleseismic anisotropic tomography using an eikonal solver and adjoint method images the Valles Caldera (VC) magmatic system
- A pronounced low P wave velocity anomaly confirms the presence of a crustal magma chamber beneath the VC
- Strong P wave radial anisotropy within the magma chamber reveals a layered sill complex related to magma accumulation

Supporting Information:

Supporting Information may be found in the online version of this article.

Correspondence to:

G. Guo,
guogaoshan1993@gmail.com

Citation:

Guo, G., Lan, H., Xu, T., & Liu, Q. (2026). Teleseismic radial anisotropy reveals a sill-dominated magma reservoir beneath the Valles Caldera, New Mexico. *Geophysical Research Letters*, *53*, e2025GL120000. https://doi.org/10.1029/2025GL120000

Received 13 NOV 2025
Accepted 4 MAR 2026

Author Contributions:

Conceptualization: Gaoshan Guo
Methodology: Gaoshan Guo
Supervision: Haiqiang Lan, Qinya Liu
Visualization: Tao Xu
Writing – original draft: Gaoshan Guo
Writing – review & editing: Gaoshan Guo, Haiqiang Lan, Tao Xu, Qinya Liu

Abstract The Valles Caldera (VC), one of the largest Quaternary silicic calderas in North America, formed by explosive rhyolitic eruptions. Seismic studies suggest a crustal magmatic reservoir beneath the caldera with low-velocity anomalies, but resolving the detailed geometry of localized melt requires constraints from seismic anisotropy. To image P-wave velocity and radial anisotropy using dense nodal array data, we develop a teleseismic tomography method that integrates an eikonal solver with the adjoint-state approach. Our results reveal a pronounced low-velocity anomaly (>20% reduction) extending laterally across the resurgent dome and down to 15–20 km depth, consistent with a crustal magma chamber. We also identify a colocated zone showing a previously unrecognized pattern of strong positive P-wave radial anisotropy (up to 8%) where horizontally polarized P-waves travel faster than vertically polarized ones. This anisotropy indicates a laterally extensive magmatic sill complex and provides new constraints on magma distribution and reservoir architecture beneath the VC.

Plain Language Summary The Valles Caldera (VC) in New Mexico is a large volcanic crater formed by past explosive eruptions. While it is well established that a magma reservoir exists beneath the caldera, how this magma is stored underground remains unclear. In this study, we used seismic waves from distant earthquakes (teleseismic waves) recorded by recently deployed dense arrays of seismometers to construct a 3D image of the magmatic reservoir. We discovered a large region with unusually low seismic velocities and strong directional differences in wave speeds, suggesting the presence of partially molten rock stored in horizontal layers. These findings indicate that magma beneath the VC is organized as a sill complex, a structure that may influence how magma accumulates and eventually erupts. This improved understanding of the reservoir architecture has important implications for assessing the dynamics and potential hazards of future eruptions.

1. Introduction

The three largest Quaternary calderas in North America, Yellowstone (YS), Long Valley (LV), and Valles Caldera (VC) have experienced explosive eruptions and sustained magmatic activity (Figure 1a). These volcanic centers serve as key natural laboratories for investigating magma storage, crust–mantle interactions, and the dynamics of continental extension (Schmandt et al., 2019). Among them, the VC is located within the Jemez Volcanic Field (JVF) in northern New Mexico (Figure 1b). It formed during two massive rhyolitic eruptions at approximately 1.6 Ma and 1.23 Ma, and is widely regarded as a classic example of a resurgent caldera characterized by a resurgent dome, Redondo Peak (Figure 1c). Although its geological record provides a clear account of past caldera-forming processes, the present-day state of the underlying magmatic system remains uncertain (Wilgus et al., 2023). To better constrain the current magmatic structure beneath the caldera, seismic imaging provides a powerful means of investigation.

Previous seismic investigations, ranging from the Jemez Tomography Experiment (JTEX) in the 1990s (Aprea et al., 2002; Roberts et al., 1995; Steck et al., 1998) to recent deployments of dense nodal array (Wilgus et al., 2023), have revealed anomalous velocity and attenuation beneath the VC. These results consistently point to the existence of a crustal magma reservoir, yet the fine-scale geometry and physical state of the melt remain poorly constrained. Seismic anisotropy provides a means to overcome this limitation. In particular, radial anisotropy, which distinguishes between vertically and horizontally polarized waves, is sensitive to the cumulative effects of small-scale melt features such as sills and dikes (Schmandt et al., 2019). Strong positive shear-

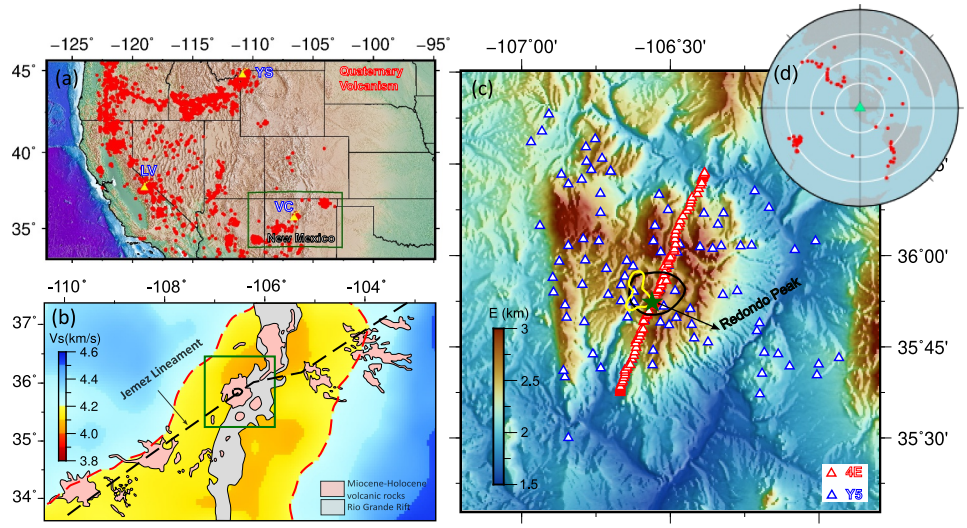

Figure 1. (a) Topographic map of the western United States with locations of Quaternary volcanism (red dots) (Walker et al., 2006). (b) Simplified tectonic map of the study area showing the V_s model at 75 km depth (Shen & Ritzwoller, 2016). Regions with $V_s \leq 4.2$ km/s, indicative of partial melt (Schmandt et al., 2019). (c) Detailed map of the Valles Caldera (VC). Red- and blue-edged triangles mark the Valles 3C transect (network 4E) (Schmandt, 2019) and the VC–Gallina Fault Array (network Y5) (Schmandt & Chaput, 2021), respectively. The black line shows the 1.23 Ma ring fracture; the yellow line outlines geothermal gradients >300°C/km (Morgan et al., 1996). The green star marks Redondo Peak. (d) Polar projection showing the 74 teleseismic events (red dots) used in the inversion; the green triangle marks the center of the study area.

wave radial anisotropy was first reported beneath the Toba Caldera (Jaxybulatov et al., 2014) and interpreted as evidence for a crustal-scale sill complex, consistent with incremental models of magma accumulation through repeated sill intrusions (Annen et al., 2006). Similar signatures have since been documented beneath YS and LV (Jiang et al., 2018; Wu et al., 2023). For the VC, whether comparable anisotropic structures exist remained uncertain for a long time. Recently, Song et al. (2026) presented the first S-wave anisotropic model beneath the VC, providing compelling evidence for anisotropic structure consistent with a silicic magma reservoir. To date, all studies have focused on S-wave anisotropy imaged by ambient-noise tomography, leaving the potential of P-wave anisotropy largely unexplored (Schmandt et al., 2019).

To address these issues, we image the P-wave radial anisotropic structure beneath the VC by recently deployed dense seismic nodal arrays using teleseismic tomography (Figure 1c). Although teleseismic tomography has traditionally been applied to mantle-scale imaging, its application to crustal-scale structures remains rare (Terhemba et al., 2022; Yao et al., 2025). A key advantage is that teleseismic waveforms exhibit high similarity, allowing for precise phase picking, while their long ray paths sample the full crustal column (Bai et al., 2020). Our inversion framework builds on a recently developed approach (Guo et al., 2025) that combines an efficient eikonal solver with the adjoint-state method, enabling stable gradient-based inversion of strongly heterogeneous media and straightforward extension to anisotropic cases (Li et al., 2022; Rawlinson et al., 2006; Tong, 2021). The computational cost depends on the number of distant earthquakes rather than the number of stations, making this method particularly well suited for dense nodal arrays.

The paper is organized as follows. We first summarize the geological and geophysical setting of the VC region. Next, we describe the anisotropic teleseismic tomography, including the forward modeling and inversion scheme. We then present and interpret the results for P-wave velocity structures and radial anisotropy of the crust beneath the caldera in comparison with previous studies. Finally, we discuss the implications for magmatic processes and outline key perspectives for future research.

2. Geological and Geophysical Setting

The VC formed at the intersection of the north-trending Rio Grande Rift (RGF) and the northeast-trending Jemez Lineament, a prominent volcanic chain within the JVF. Rifting initiated at about 25 Ma (Ricketts et al., 2016), and volcanism in the JVF began near 16 Ma, evolving from mafic to more silicic compositions after 7–8 Ma as crustal

melting became increasingly significant (Goff et al., 2011). Two major eruptions of the Bandelier Tuff produced the Toledo Caldera at ∼1.6 Ma and the VC at ∼1.23 Ma. Redondo Peak rose shortly after the 1.23 Ma collapse as a resurgent dome, recording renewed magmatic intrusion and pressurization, accompanied by extensive rhyolite emplacement along the ring fracture between ∼1.23 and 0.5 Ma (Kennedy et al., 2012). Late-stage activity, including the El Cajete pyroclastic deposits (∼74 ka) and the Banco Bonito lava flow (∼69 ka), reflects episodic rejuvenation of the shallow magma reservoir (Nasholds & Zimmerer, 2022).

Despite its extensive eruptive history, the VC shows little evidence of current volcanic unrest compared with the YS and LV. Seismicity within the caldera is sparse, in contrast to the moderate levels observed in the surrounding regions (House & Roberts, 2019), and no significant geodetic deformation or seismic velocity variations have been detected (Maier et al., 2025). The paucity of earthquakes likely reflects ductile deformation facilitated by elevated subcaldera crustal temperatures, reaching up to 350°C (Morgan et al., 1996) (Figure 1c), as a result of episodic volcanism and repeated magma intrusion over the past 13 Myr. These temperatures substantially exceed those estimated at the LV (∼130°C; Hurwitz et al. (2010)) and YS (240–340°C; Dobson et al. (2003); Hurwitz and Lowenstern (2014)). Alternatively, the lack of seismicity may result from a stable cooling reservoir and the absence of active triggering processes such as magma intrusion, fluid pressurization, or gas migration (Maier et al., 2025).

Seismic imaging nevertheless provides compelling evidence for a crustal magma system beneath the VC. Early evidence came from a joint inversion of local earthquake and explosion traveltimes, which revealed a ∼15 km-wide low-velocity zone beneath the caldera, with P-wave velocities up to 7% lower than the surrounding crust (Ankeny et al., 1986). Subsequent investigations during the JTEX experiment confirmed this feature through P-wave tomography, resolving a vertically elongated, ellipsoidal low-Vp anomaly with reductions of up to 23% (Steck et al., 1998). Using the same data set, Aprea et al. (2002) imaged abrupt interfaces from backscattered teleseismic P waves and revealed pronounced attenuation anomalies (Roberts et al., 1995), suggesting strong heterogeneity in the shallow crust. After a long dormant period in seismic monitoring, the region has regained attention with the deployment of the Valles 3C Node Transect (Schmandt, 2019) and the VC–Gallina Fault Array (Schmandt & Chaput, 2021). Ambient-noise tomography using these nodal arrays has identified complementary S-wave velocity and radial-anisotropy structures, including a colocated low-Vs anomaly with velocity reduction of ∼32% (Wilgus et al., 2023) and a radial-anisotropy increase exceeding 15% (Song et al., 2026). Together, these findings point to the presence of partial melt in the upper crust and provide key geophysical constraints on the present-day magmatic system beneath the VC.

3. Method

Teleseismic tomography that integrates the eikonal solver and the adjoint-state technique has been developed in two different formulations by Chen et al. (2023) and Guo et al. (2025), respectively. Both implementations share a unified theoretical framework that originated in exploration seismology (Guo et al., 2022; Leung & Qian, 2006). Here, we extend it to jointly invert for velocity and radial anisotropy using relative teleseismic arrivals.

3.1. Eikonal Equation for Radially Anisotropic Media

Teleseismic P-wave traveltimes in a radially anisotropic medium are obtained by solving

$$\begin{cases} \nabla t_s(\mathbf{x})\, r(\mathbf{x})\, \nabla t_s(\mathbf{x})^{\mathrm{T}} = 1, & \mathbf{x} \in \Omega, \\ t_s(\mathbf{x}_s) = g(\mathbf{x}_s), & \mathbf{x}_s \in \Gamma, \end{cases} \tag{1}$$

where $r(\mathbf{x}) = \mathrm{diag}\left(v_{pv}^2(\mathbf{x}), v_{ph}^2(\mathbf{x}), v_{ph}^2(\mathbf{x})\right)$ defines vertical and horizontal P-wave velocities v_{pv} and v_{ph}, respectively and $g(\mathbf{x}_s)$ specifies the analytical traveltime at the lower boundary Γ (Text S1 in Supporting Information S1 for details) from AK135 Earth model (Kennett et al., 1995). This equation is solved using the lock sweeping method (Zhou et al., 2023), and simulated traveltimes are interpolated to receiver positions using B-splines:

$$t_{s,r} = B_{s,r}, t_s(\mathbf{x}). \tag{2}$$

To reduce the influence of structures outside the model domain, we define relative traveltime residuals (Rawlinson et al., 2006) as

$$d_{s,r} = \left(t_{s,r} - t^{\mathrm{ref}}_{s,r}\right) - \frac{1}{N^s_r}\sum_{r=1}^{N^s_r}\left(t_{s,r} - t^{\mathrm{ref}}_{s,r}\right), \tag{3}$$

where $t^{\mathrm{ref}}_{s,r}$ is predicted by a reference model and N^s_r is the number of arrivals for event s.

3.2. Adjoint-State Method for Teleseismic Radial Anisotropy Tomography

The damped least-squares misfit function for teleseismic tomography is defined as:

$$\mathcal{J}(\mathbf{m}) = \frac{1}{2}\sum_{s=1}^{N_s}\sum_{r=1}^{N^s_r}\left(\frac{d^*_{s,r} - d_{s,r}(\mathbf{m})}{C^d_{s,r}}\right)^2 + \frac{\epsilon}{2}\sum_{i=1}^{N_M}\left(\frac{m(x_i) - m^{ref}(x_i)}{C^M_i}\right)^2, \tag{4}$$

where $\mathbf{m} = (v_{pv}(\mathbf{x}), v_{ph}(\mathbf{x})) = \sum_{i=1}^{N_M} m(x_i)$ denotes the model parameters to be updated, $d^*_{s,r}$ and $d_{s,r}(\mathbf{m})$ are the observed and predicted relative traveltime residuals, C^d and C^M are the data and model covariance terms, and ϵ is a regularization factor. The gradient of the misfit is computed following the adjoint-state method (Plessix, 2006), by solving:

$$\nabla\cdot(-\lambda_s(\mathbf{x})r(\mathbf{x})\nabla t_s(\mathbf{x}))_\Omega = \sum_{r=1}^{N^r_s} B^T_{s,r}\frac{d_{s,r}(\mathbf{m}) - d^*_{s,r}}{\left(C^d_{s,r}\right)^2}\left(1 - \frac{1}{N^s_r}\right), \tag{5}$$

where λ_s is the adjoint field. Once λ_s is obtained (Text S1 in Supporting Information S1), the gradient with respect to v_{pv} and v_{ph} is:

$$\frac{\partial\mathcal{J}}{\partial v_{pv}(\mathbf{x})} = v_{pv}(\mathbf{x})\sum_{s=1}^{N_s}\lambda_s(\mathbf{x})t^r_s(\mathbf{x})^2, \tag{6a}$$

$$\frac{\partial\mathcal{J}}{\partial v_{ph}(\mathbf{x})} = v_{ph}(\mathbf{x})\sum_{s=1}^{N_s}\lambda_s(\mathbf{x})\left(t^\theta_s(\mathbf{x})^2 + t^\phi_s(\mathbf{x})^2\right). \tag{6b}$$

We update the model using a preconditioned L-BFGS algorithm (Métivier & Brossier, 2016) within the framework of adjoint-state simulation (Guo et al., 2025; Zhang et al., 2025). Finally, the averaged isotropic velocity (v_{pmean}) and radial anisotropy (β) are defined as (Hu et al., 2020):

$$v_{\mathrm{pmean}}(\mathbf{x}) = \frac{v_{pv}(\mathbf{x}) + v_{ph}(\mathbf{x})}{2}, \tag{7a}$$

$$\beta(\mathbf{x}) = \frac{v_{ph}(\mathbf{x}) - v_{pv}(\mathbf{x})}{v_{\mathrm{pmean}}(\mathbf{x})}. \tag{7b}$$

4. Data Processing and Tomographic Results

4.1. Data Set

To investigate the 3D crustal structure beneath the VC, we analyzed teleseismic waveforms recorded by 189 nodal seismometers deployed across two temporary arrays (Figure 1c). The first array, the Valles 3C Node Transect, consisted of 97 nodes along a ~70 km SSW–NNE line crossing the VC center and operated for one month during October–November 2019 (Schmandt, 2019). The second array, the VC–Gallina Fault Array, comprised 72 nodes in a 2D layout extending the transect and was deployed for one month during September–October 2021 (Schmandt & Chaput, 2021). The transect has been used by Wilgus et al. (2023) to obtain a V_s profile, and

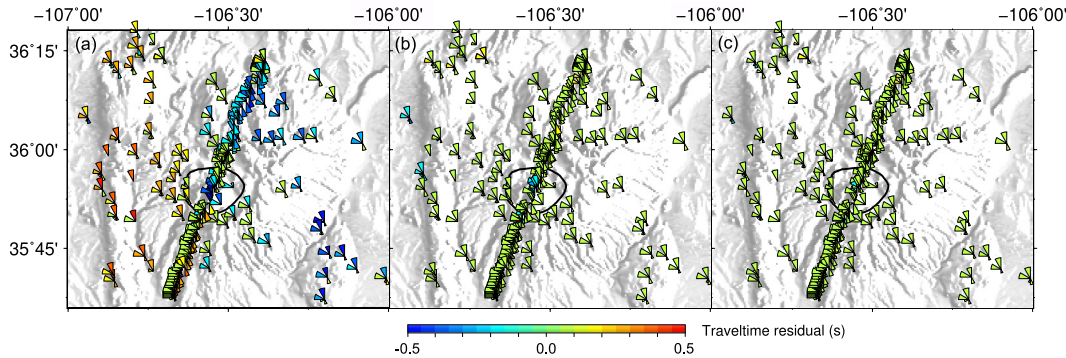

Figure 2. Sector diagrams of azimuthally averaged relative traveltime anomalies. (a) Observed anomalies before inversion. (b) After isotropic inversion. (c) After radial anisotropic inversion. Each sector diagram represents normalized relative traveltime anomalies within a 30° back-azimuth window at each station. The sector length denotes the number of measurements, and the color indicates the average relative traveltime anomaly. The black line outlines the 1.23 Ma caldera ring fracture. The plotting is inspired by Liang et al. (2016).

combined data sets were subsequently used by Song et al. (2026) to infer 3D V_s and radial anisotropy from ambient-noise tomography. Wilgus et al. (2023) also analyzed P-wave arrivals from a single teleseismic event to infer a low-velocity magma reservoir, although no tomographic inversion was performed. To address these limitations, we incorporated many more teleseismic events and carried out a full 3D tomographic inversion using data from both arrays. Raw waveforms were corrected for instrument response, mean, and linear trend, and band-pass filtered between 0.1 and 2.0 Hz. We selected earthquakes with magnitudes greater than 4.6 that generated clear direct P-wave arrivals at no fewer than four stations at epicentral distances of 30°–94° (Figure 1d). The final data set contains 2,797 relative P-wave traveltime residuals from 74 teleseismic events. Traveltimes were manually picked using waveform stacking and multichannel cross-correlation (Lou et al., 2013).

4.2. Inversion Configuration

For radially anisotropic tomography, trade-offs between 3D isotropic heterogeneity and radial anisotropy are a key challenge. To reduce this ambiguity, we adopt a two-step inversion strategy. We first invert for an isotropic model until further misfit reduction becomes negligible, and then introduce radial anisotropy by jointly solving for the horizontal and vertical P-wave velocity components. We subsequently compute the isotropic velocity and radial-anisotropy parameters using Equation 7. Details of the model configuration and damping selection are provided in Texts S2 and S3 of Supporting Information S1.

The inversion performance is further evaluated using azimuthally averaged relative traveltime residuals (Figure 2). The observed residuals (Figure 2a) show that the negative delay times correspond to negative velocity anomalies in the east, whereas positive delays indicate positive velocity anomalies in the west. In the center of the VC, strong negative delays reveal a pronounced low-velocity anomaly. After isotropic inversion, delay times are significantly reduced at most stations; however, strong negative delays persist at the VC center (Figure 2b), suggesting that the structure cannot be fully explained by isotropy alone and motivating the implementation of radial anisotropy inversion. As expected, delay times at the VC center are further reduced after anisotropic inversion, highlighting the presence of radial anisotropy beneath the caldera (Figure 2c). Several stations along the western margin also display delay patterns, possibly related to anisotropic structure, but these are not discussed in detail due to edge effects.

4.3. Averaged Isotropic Velocity and Radial Anisotropy From Teleseismic Tomography

The results of the teleseismic isotropic inversion are presented in Text S4 of Supporting Information S1. These results exhibit large-scale features similar to the averaged velocity model from the anisotropic inversion. Therefore, our analysis primarily focuses on the radial anisotropic inversion results presented in Figure 3, revealing prominent P-wave velocity and anisotropy anomalies beneath the VC. At 8 km depth, the northeastern portion of the model is generally characterized by low P-wave velocities, whereas the southwestern portion exhibits relatively higher velocities (Figure 3a). This large-scale east–west contrast is a first-order feature of the

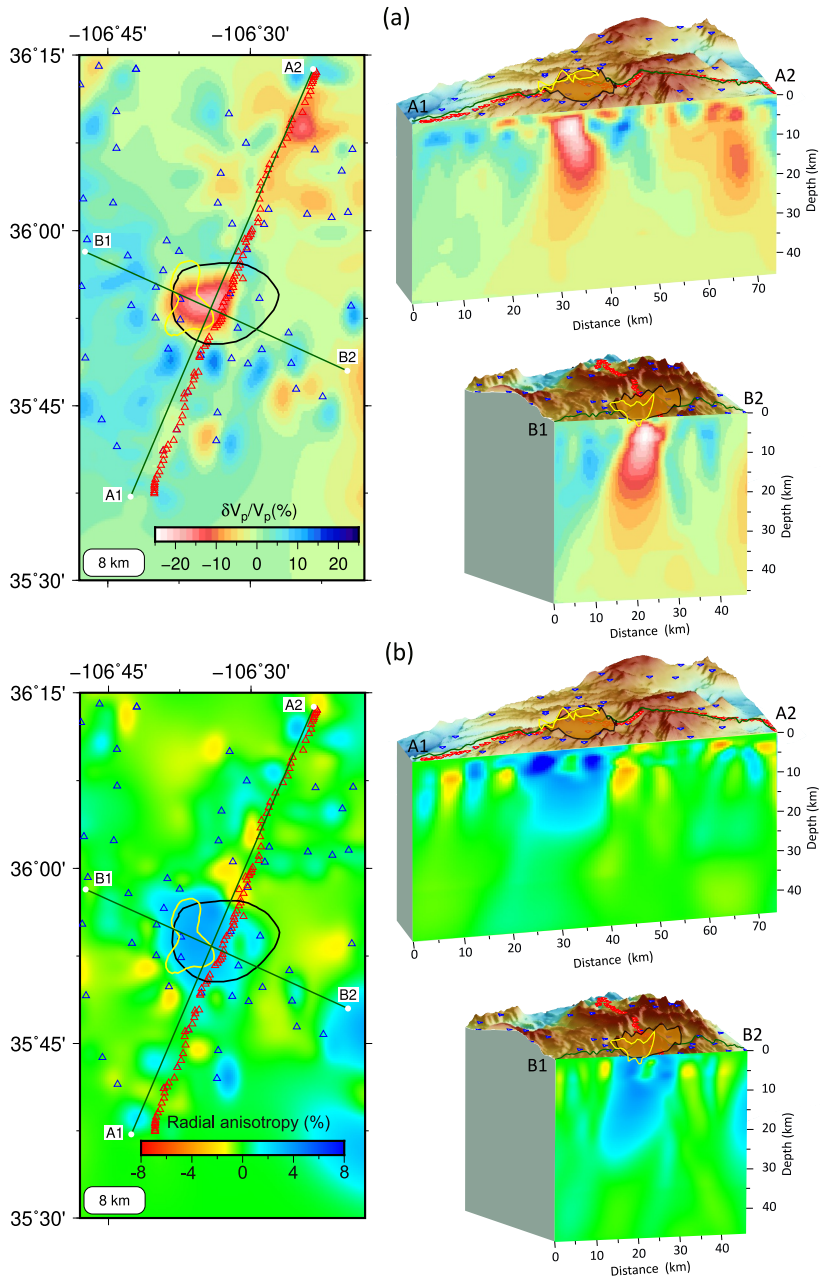

Figure 3. Results of teleseismic radial anisotropic inversions beneath the linear Valles Caldera nodal array. (a) Horizontal slice of P-wave averaged velocity perturbations at 8 km depth and vertical cross-sections along profiles A1–A2 and B1–B2, respectively. (b) Horizontal slice of radial anisotropy at the same depth and corresponding vertical cross-sections. Triangles denote seismic stations. The surface trace of the ring fracture is indicated by the black line and by the black lines shaded in dark yellow. The yellow contour outlines the area with geothermal gradients ≥350°C/km. Topography is projected above each vertical cross-section for reference. Green lines in each panel show the positions of profiles A1–A2 and B1–B2.

velocity model. However, due to the sparse two-dimensional distribution of seismic stations outside the main NS linear array, we refrain from overinterpreting this lateral variation, as the resolution in peripheral areas is likely limited. More locally, a pronounced low-velocity zone is observed beneath the resurgent dome, Redondo Peak of northwestern VC region (Figure 1c), with P-wave velocity perturbations reaching up to −20% (Figure 3a). This low-velocity feature is laterally extensive and vertically continuous down to 15–20 km depth, as shown in the A1–A2 and B1–B2 cross-sections. In parallel, the radial anisotropy at the same depth (depth 8 km in Figure 3b) shows

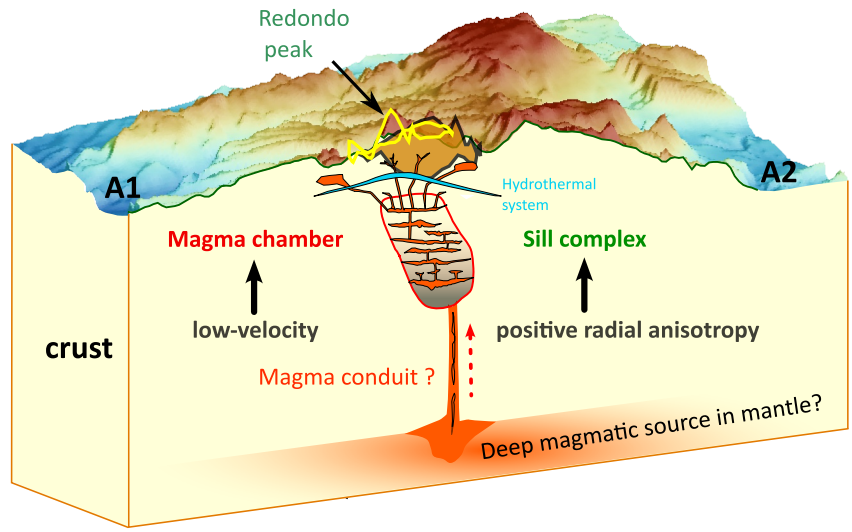

Figure 4. Conceptual cross-section of the magmatic system beneath the Valles Caldera, constrained by seismic observations. A sill complex, inferred from zones of low seismic velocity and strong positive radial anisotropy, intrudes laterally into the upper crust and supplies fluids to the overlying hydrothermal system. A deeper magmatic source in the mantle may act as the ultimate feeder through a magma conduit. The resurgent dome, Redondo Peak, is shown at the surface.

strong positive values (up to 8%), indicating a significant contrast between horizontally and vertically polarized P-wave velocities. The high-anisotropy anomalies are concentrated beneath the VC and persist in depth along both cross-sections (Figure 3b), spatially coinciding with the low P-velocity zones. The observed colocation of low P velocities and strong radial anisotropy outlines a distinct structural domain in the upper to middle crust beneath the VC.

4.4. Assessing Resolution Through Checkerboard and Recovery Tests

The anisotropic inversion shows a weak, first-order lateral gradient in the averaged P-wave velocity perturbations across the model domain. More robustly, it images a pronounced low-velocity anomaly and strong positive radial anisotropy beneath the VC. Given the predominantly steep incidence angles of teleseismic P waves, the data are generally more sensitive to v_{pv} than to v_{ph}, which may lead to trade-offs between 3D isotropic heterogeneity and inferred radial anisotropy. We therefore evaluate model resolution and parameter assessment using checkerboard (Text S6 in Supporting Information S1) and recovery tests (Text S7 in Supporting Information S1). As shown in Figures S5–S7 in Supporting Information S1, the first-order lateral velocity pattern, along with the low-velocity anomaly and positive radial anisotropy, is well recovered. Although the velocity perturbations are damped with depth, the anisotropic features are better preserved. We also show ray density and distribution for both the initial and final models to illustrate the illumination provided by teleseismic data (Figures S8–S9 in Supporting Information S1). The results confirm that the VC is well illuminated along the main profile, supporting the robustness of the low-velocity and radial anisotropy.

5. Discussion

The first-order velocity anomaly pattern, negative in the northeast and positive in the southwest flank of the VC, is consistent with the S-wave velocity structure along the VC transect (Wilgus et al., 2023). This may result from mid-Miocene intermediate-to-mafic volcanism on the northeastern flank where extrusive rocks could reduce upper crustal velocities, in contrast to the southwestern side. In the following, we mainly focus on the central low-Vp anomaly and positive radial anisotropy beneath VC, and their implications for the present magmatic system.

5.1. Middle-to-Upper Crustal Magmatic Sill Complex Beneath the VC

The spatial correlation between pronounced low P-wave velocity anomalies and strong radial anisotropy beneath the VC provides compelling evidence for a laterally extensive magmatic sill complex within the middle to upper crust, as illustrated in Figure 4. This interpretation follows the model proposed by Annen et al. (2006) and is

consistent with recent observations beneath the Toba (Jaxybulatov et al., 2014; Wang et al., 2025), YS, and LV calderas (Jiang et al., 2018; Wu et al., 2023). We further discuss our results in the context of this model, considering the velocity and anisotropy structures separately.

As shown in Figure 3a, the depth range of this low-velocity anomaly beneath the VC overlaps the petrologically estimated storage depths of erupted rhyolites (2.5–9 km) (Huang et al., 2015), suggesting that the observed velocity depression represents a partially molten or highly fractured magmatic body (Figure 4). This interpretation is consistent with previous studies that attributed similar low-velocity features beneath large caldera systems to melt-rich sills or intrusions (Jiang et al., 2018; Maguire et al., 2022). The location and magnitude of the P anomaly beneath the VC in our images are generally consistent with a comparable feature with maximum Vp reductions of ∼23% by teleseismic tomography of JTEX (Steck et al., 1998). Based on a recent S-wave velocity model, the corresponding velocity perturbation within this volume reaches about 32% (Wilgus et al., 2023). The greater reduction in S-wave velocity likely reflects the higher sensitivity of shear waves to partial melt which strongly reduce the shear modulus but have a smaller effect on the bulk modulus. Spatially, the low-velocity anomaly exhibits a slight asymmetry, rising from beneath the central sector toward the north-northwestern rim of the caldera. The location of this feature agrees well with Steck et al. (1998), although its lateral extent differs slightly, likely reflecting the denser spatial sampling provided by the node array used in this study, which yields a substantially improved constraint on the geometry of the anomaly. The depth extent of the low-velocity zone remains uncertain, as the predominantly vertical propagation of teleseismic rays limits vertical resolution. Nevertheless, the overall depth distribution is broadly consistent with the S-wave velocity model (Wilgus et al., 2023).

The positive radial anisotropy anomaly exhibits amplitudes of up to 8% in the shallow crust along profile A (Figure 3b), decreasing to approximately 4% within the middle crust. Spatially, this anisotropy anomaly coincides with the low-velocity anomaly, but displays a somewhat broader lateral extent. This pattern likely reflects horizontally aligned melt-filled cracks or layered intrusive bodies that enhance horizontal relative to vertical P-wave velocities. This anisotropic signature points to a sill-dominated magmatic architecture, where repeated emplacement of subhorizontal intrusions gives rise to a laminated crustal structure (Figure 4). To our knowledge, this represents the first observation of P-wave radial anisotropy associated with a magma chamber beneath the caldera. Importantly, it is consistent with the recent ambient-noise S-wave model that reports strong positive radial anisotropy exceeding 15% beneath the VC (Song et al., 2026). Analogous S-wave studies in other caldera systems also show pronounced positive radial anisotropy above crustal magma reservoirs. For example, Jaxybulatov et al. (2014) first reported a positive S-wave radial anisotropy anomaly beneath the Toba caldera, which was later re-evaluated by Wang et al. (2025) using advanced waveform tomography, yielding an anisotropy of nearly 30%. Comparable anomalies, with mean strengths of 8% in LV and 12% in YS at depths of 5–18 km, were documented by Jiang et al. (2018). More recently, this anisotropy beneath YS was re-evaluated by Wu et al. (2023) using a denser nodal array, yielding a higher estimate of about 20% at the top of the reservoir. Although the inferred anisotropy amplitudes vary due to differences in data coverage and inversion methodology, all consistently indicate pronounced positive radial anisotropy associated with crustal magma reservoirs. Overall, the P-wave radial anisotropy beneath the VC reveals a sill-dominated magma system formed by subhorizontal intrusions, consistent with S-wave anisotropy patterns in other large calderas and reflecting a common process of magma accumulation in the middle-to-upper crust.

The shallow (0–5 km) low-velocity but comparatively weak and spatially heterogeneous signal (Figures 3a and 3b) may reflect a transition from intrusion-dominated fabric at mid-crustal levels to hydrothermal alteration and fracture-controlled properties in the uppermost crust. In this zone, pervasive alteration, elevated pore-fluid pressure, and dense fracturing can reduce V_p, whereas the net radial-anisotropy signal may remain modest if fractures are variably oriented or heterogeneous over length scales smaller than our resolution. This interpretation is consistent with a dynamically coupled magmatic–hydrothermal system (Wilks et al., 2020).

5.2. Implications for the Magmatic System of the VC

The integrated tomographic and interpretive results (Figure 4) indicate that the current VC magmatic system comprises a vertically connected network linking a possible deep magmatic source in the upper mantle to a middle-to-upper crustal sill complex and an overlying hydrothermal system. To better understand magma storage

conditions and assess the likelihood of future eruptions beneath the VC, it is essential to quantify the total melt content. Although there are significant uncertainties in estimating the melt fraction and volume from seismic tomography alone (Paulatto et al., 2022), our P-wave model provides a first-order approximation of the average melt fraction within the VC magma reservoir. Following Huang et al. (2015), we adopt a 7% v_{pmean} reduction as a proxy for partial melt in the middle to upper crust and estimated the anomaly volume by integrating the 3D grid cells that satisfy a prescribed velocity-reduction threshold 7% in the tomographic model. Using this threshold-based approach, we obtain a low-velocity anomaly volume of ∼1450 km^3 for the largest connected low-velocity body (363 grid cells; ∼4 km^3 per cell), comparable to the partially molten volume of ∼1,200 km^3 inferred from the recent S-wave model (Song et al., 2026). Using the approach of Chu et al. (2010) developed for the YS system, we estimate the melt fraction beneath the VC. The background velocity increases gradually from ∼5.8 km/s at 2 km depth to 6.5 km/s at 30 km, whereas the average isotropic P-wave velocity within the anomalous zone is approximately 4.6–5.2 km/s, yielding an average melt fraction of about 9%–18%. This corresponds to an estimated melt volume of ∼130.5–261 km^3 distributed within a 1,450 km^3 domain extending from the surface to ∼20 km depth (Figure 4). This estimate is also consistent with the ∼100–200 km^3 melt volume inferred from the S-wave model (Song et al., 2026). Considering the strong damping of the P-wave velocity model in teleseismic tomography, this estimate likely represents a lower bound (Lin et al., 2014) and is therefore comparable to the 17%–22% inferred from the S-wave model.

These melt fractions for the VC magmatic system are likely lower than those that prevailed prior to past eruptions, as most erupted rhyolites contained 35%–55% crystal cargo (Myers et al., 2016; Wu et al., 2023). This comparison suggests that the present-day VC reservoir lacks the melt-rich domains that characterized its pre-eruptive state, indicating that it is not currently in an eruptible condition. This inference is consistent with the limited seismicity and the absence of measurable surface deformation. Nevertheless, our eikonal-based inversion likely underestimates the true magnitude of the low-velocity anomaly and consequently the melt fraction. Future studies that jointly invert P- and S-wave velocities, anisotropy, and attenuation using advanced waveform-based tomography (Wang et al., 2021; Xu et al., 2025) will be essential for constraining melt, fluid, and gas fractions, thereby refining our understanding of the mush-dominated magma reservoir beneath the VC.

6. Conclusions

We present the first anisotropic P-wave velocity model for the VC, New Mexico, derived from a teleseismic tomography approach. The observed pronounced low P-velocity anomaly and positive radial anisotropy indicate the presence of a magmatic sill complex beneath the VC. This structure, likely formed by horizontally layered melt accumulations, may play a key role in magma storage and transport. Our results demonstrate the capability of teleseismic anisotropic imaging using dense nodal arrays to resolve the detailed architecture of magmatic reservoirs. However, the absolute amplitudes of the velocity and anisotropy anomalies remain uncertain. Future studies incorporating multiparameter inversions within advanced waveform tomography frameworks will further constrain the melt fraction and physical properties of the magmatic system.

Acknowledgments
We thank Editor Germán Prieto and two anonymous reviewers for their constructive comments. We also thank Prof. Brandon Schmandt and the field crews for deploying the Valles 3C Node Transect and the Valles Caldera–Gallina Fault Array, and for making the data openly available through EarthScope. We thank Lingkai Meng for help with data processing and Dr. Akram Mostafanejad for discussions of the VC data set. G. Guo and Q. Liu were supported by the Natural Sciences and Engineering Research Council of Canada (NSERC) Discovery Grant (Individual). H. Lan was supported by the National Key R&D Program of China (Grant 2023YFF0803500) and the Strategic Priority Research Program (B) of the Chinese Academy of Sciences (Grant XDB24000000).

Conflict of Interest

The authors declare no conflicts of interest relevant to this study.

Availability Statement

The seismic waveforms from the VC node arrays (networks Y5 and 4E) were obtained from the IRIS Data Services (Schmandt, 2019; Schmandt & Chaput, 2021). Data processing was conducted using ObsPy (Beyreuther et al., 2010) and AIMBAT (Lou et al., 2013), while most figures were created with GMT (Wessel et al., 2019). The code package developed in this study is available on Zenodo (Guo, 2025).

References

Ankeny, L., Braile, L., & Olsen, K. (1986). Upper crustal structure beneath the Jemez Mountains volcanic field, New Mexico, determined by three-dimensional simultaneous inversion of seismic refraction and earthquake data. *Journal of Geophysical Research*, *91*(B6), 6188–6198. https://doi.org/10.1029/JB091iB06p06188

Annen, C., Blundy, J., & Sparks, R. (2006). The genesis of intermediate and silicic magmas in deep crustal hot zones. *Journal of Petrology*, *47*(3), 505–539. https://doi.org/10.1093/petrology/egi084

Aprea, C. M., Hildebrand, S., Fehler, M., Steck, L., Baldridge, W. S., Roberts, P., et al. (2002). Three-dimensional Kirchhoff migration: Imaging of the Jemez volcanic field using teleseismic data. *Journal of Geophysical Research*, *107*(B10), ESE11-1–ESE11-15. https://doi.org/10.1029/2000JB000097

Bai, T., Thurber, C., Lanza, F., Singer, B. S., Bennington, N., Keranen, K., & Cardona, C. (2020). Teleseismic tomography of the Laguna del Maule volcanic field in Chile. *Journal of Geophysical Research: Solid Earth*, *125*(8), e2020JB019449. https://doi.org/10.1029/2020jb019449

Beyreuther, M., Barsch, R., Krischer, L., Megies, T., Behr, Y., & Wassermann, J. (2010). Obspy: A python toolbox for seismology. *Seismological Research Letters*, *81*(3), 530–533. https://doi.org/10.1785/gssrl.81.3.530

Chen, J., Wu, S., Xu, M., Nagaso, M., Yao, J., Wang, K., et al. (2023). Adjoint-state teleseismic traveltime tomography: Method and application to Thailand in Indochina Peninsula. *Journal of Geophysical Research: Solid Earth*, *128*(12), e2023JB027348. https://doi.org/10.1029/2023jb027348

Chu, R., Helmberger, D. V., Sun, D., Jackson, J. M., & Zhu, L. (2010). Mushy magma beneath Yellowstone. *Geophysical Research Letters*, *37*(1), L01306. https://doi.org/10.1029/2009gl041656

Dobson, P. F., Kneafsey, T. J., Hulen, J., & Simmons, A. (2003). Porosity, permeability, and fluid flow in the Yellowstone geothermal system, Wyoming. *Journal of Volcanology and Geothermal Research*, *123*(3–4), 313–324. https://doi.org/10.1016/s0377-0273(03)00039-8

Goff, F., Gardner, J. N., Reneau, S. L., Kelley, S. A., Kempter, K. A., & Lawrence, J. R. (2011). Geologic map of the Valles caldera, Jemez mountains, New Mexico. *New Mexico Bureau of Geology and Mineral Resources Geologic Map*, *79*(scale 1), 50.

Guo, G. (2025). Teleseismic traveltime tomography for radial anisotropic media [Software]. *Zenodo*. https://doi.org/10.5281/zenodo.17575186

Guo, G., Lan, H., Chen, L., Meng, L., & Badal, J. (2025). Lithospheric thinning of the Northeastern Arabian margin revealed by matrix-free teleseismic traveltime tomography. *Geophysical Research Letters*, *52*(3), e2024GL112604. https://doi.org/10.1029/2024GL112604

Guo, G., Lan, H., Zhou, X., Liu, Y., Waheed, U. B., & Chen, J. (2022). Topography-dependent eikonal tomography based on the fast-sweeping scheme and the adjoint-state technique. *Geophysics*, *87*(2), U29–U41. https://doi.org/10.1190/geo2021-0116.1

House, L., & Roberts, P. (2019). Seismicity monitoring in North-Central New Mexico by the Los Alamos seismic network. *Seismological Research Letters*, *91*(2A), 593–600. https://doi.org/10.1785/0220190208

Hu, S., Yao, H., & Huang, H. (2020). Direct surface wave radial anisotropy tomography in the crust of the eastern Himalayan syntaxis. *Journal of Geophysical Research: Solid Earth*, *125*(5), e2019JB018257. https://doi.org/10.1029/2019jb018257

Huang, H.-H., Lin, F.-C., Schmandt, B., Farrell, J., Smith, R. B., & Tsai, V. C. (2015). The Yellowstone magmatic system from the mantle plume to the upper crust. *Science*, *348*(6236), 773–776. https://doi.org/10.1126/science.aaa5648

Hurwitz, S., Farrar, C. D., & Williams, C. F. (2010). The thermal regime in the resurgent dome of long Valley Caldera, California: Inferences from precision temperature logs in deep wells. *Journal of Volcanology and Geothermal Research*, *198*(1–2), 233–240. https://doi.org/10.1016/j.jvolgeores.2010.08.023

Hurwitz, S., & Lowenstern, J. B. (2014). Dynamics of the Yellowstone hydrothermal system. *Reviews of Geophysics*, *52*(3), 375–411. https://doi.org/10.1002/2014rg000452

Jaxybulatov, K., Shapiro, N. M., Koulakov, I., Mordret, A., Landès, M., & Sens-Schönfelder, C. (2014). A large magmatic sill complex beneath the Toba caldera. *Science*, *346*(6209), 617–619. https://doi.org/10.1126/science.1258582

Jiang, C., Schmandt, B., Farrell, J., Lin, F.-C., & Ward, K. M. (2018). Seismically anisotropic magma reservoirs underlying silicic calderas. *Geology*, *46*(8), 727–730. https://doi.org/10.1130/G45104.1

Kennedy, B., Wilcock, J., & Stix, J. (2012). Caldera resurgence during magma replenishment and rejuvenation at Valles and lake city calderas. *Bulletin of Volcanology*, *74*(8), 1833–1847. https://doi.org/10.1007/s00445-012-0641-x

Kennett, B. L. N., Engdahl, E. R., & Buland, R. (1995). Constraints on seismic velocities in the earth from travel times. *Geophysical Journal International*, *122*(1), 108–124. https://doi.org/10.1111/j.1365-246x.1995.tb03540.x

Leung, S., & Qian, J. (2006). An adjoint state method for three-dimensional transmission traveltime tomography using first-arrivals. *Communications in Mathematical Sciences*, *4*(1), 249–266. https://doi.org/10.4310/cms.2006.v4.n1.a10

Li, M., Liu, S., Yang, D., Xu, X., Shen, W., Xie, C., et al. (2022). Velocity structure and radial anisotropy beneath the northeastern Tibetan Plateau revealed by eikonal equation-based teleseismic P-wave traveltime tomography. *Science China Earth Sciences*, *65*(5), 824–844. https://doi.org/10.1007/s11430-021-9876-y

Liang, X., Chen, Y., Tian, X., Chen, Y. J., Ni, J., Gallegos, A., et al. (2016). 3D imaging of subducting and fragmenting Indian continental lithosphere beneath southern and central Tibet using body-wave finite-frequency tomography. *Earth and Planetary Science Letters*, *443*, 162–175. https://doi.org/10.1016/j.epsl.2016.03.029

Lin, G., Amelung, F., Lavallée, Y., & Okubo, P. G. (2014). Seismic evidence for a crustal magma reservoir beneath the upper east rift zone of Kilauea volcano, Hawaii. *Geology*, *42*(3), 187–190. https://doi.org/10.1130/G35001.1

Lou, X., van der Lee, S., & Lloyd, S. (2013). AIMBAT: A Python/Matplotlib tool for measuring teleseismic arrival times. *Seismological Research Letters*, *84*(1), 85–93. https://doi.org/10.1785/0220120033

Maguire, R., Schmandt, B., Li, J., Jiang, C., Li, G., Wilgus, J., & Chen, M. (2022). Magma accumulation at depths of prior rhyolite storage beneath Yellowstone caldera. *Science*, *378*(6623), 1001–1004. https://doi.org/10.1126/science.ade0347

Maier, N., Rodriguez, E. E., Grapenthin, R., Newman, A., Donahue, C., Lindsey, E., et al. (2025). Limited surface deformation, seismicity, and seismic velocity changes observed in Valles Caldera over decadal timescales. *Journal of Volcanology and Geothermal Research*, *460*, 108283. https://doi.org/10.1016/j.jvolgeores.2025.108283

Métivier, L., & Brossier, R. (2016). The SEISCOPE optimization toolbox: A large-scale nonlinear optimization library based on reverse communication. *Geophysics*, *81*(2), F11–F25. https://doi.org/10.1190/geo2015-0031.1

Morgan, P., Sass, J., & Jacobsen, R. (1996). Heat flow in VC-2A and VC-2B, and constraints on the thermal regime of the Valles caldera, New Mexico. In *The Jemez mountains region. New Mexico geological society 47th field conference guidebook* (pp. 231–236). New Mexico Geological Society.

Myers, M. L., Wallace, P. J., Wilson, C. J., Morter, B. K., & Swallow, E. J. (2016). Prolonged ascent and episodic venting of discrete magma batches at the onset of the Huckleberry Ridge supereruption, Yellowstone. *Earth and Planetary Science Letters*, *451*, 285–297. https://doi.org/10.1016/j.epsl.2016.07.023

Nasholds, M. W., & Zimmerer, M. J. (2022). High-precision 40Ar/39Ar geochronology and volumetric investigation of volcanism and resurgence following eruption of the Tshirege Member, Bandelier Tuff, at the Valles caldera. *Journal of Volcanology and Geothermal Research*, *431*, 107624. https://doi.org/10.1016/j.jvolgeores.2022.107624

Paulatto, M., Hooft, E. E., Chrapkiewicz, K., Heath, B., Toomey, D. R., & Morgan, J. V. (2022). Advances in seismic imaging of magma and crystal mush. *Frontiers in Earth Science*, *10*, 970131. https://doi.org/10.3389/feart.2022.970131

Plessix, R. E. (2006). A review of the adjoint-state method for computing the gradient of a functional with geophysical applications. *Geophysical Journal International*, *167*(2), 495–503. https://doi.org/10.1111/j.1365-246x.2006.02978.x

Rawlinson, N., Reading, A. M., & Kennett, B. L. N. (2006). Lithospheric structure of Tasmania from a novel form of teleseismic tomography. *Journal of Geophysical Research*, *111*(B2), B02301. https://doi.org/10.1029/2005JB003803

Ricketts, J. W., Kelley, S. A., Karlstrom, K. E., Schmandt, B., Donahue, M. S., & van Wijk, J. (2016). Synchronous opening of the Rio Grande rift along its entire length at 25–10 Ma supported by apatite (U-Th)/He and fission-track thermochronology, and evaluation of possible driving mechanisms. *Bulletin*, *128*(3–4), 397–424. https://doi.org/10.1130/b31223.1

Roberts, P. M., Aki, K., & Fehler, M. C. (1995). A shallow attenuating anomaly inside the ring fracture of the Valles Caldera, New Mexico. *Journal of Volcanology and Geothermal Research*, *67*(1), 79–99. https://doi.org/10.1016/0377-0273(94)00100-U

Schmandt, B. (2019). Valles 3C node transect [Dataset]. *IRIS Data Services*. https://doi.org/10.7914/SN/4E_2019

Schmandt, B., & Chaput, J. (2021). Valles caldera and gallina fault node array 2021 [Dataset]. *IRIS Data Services*. https://doi.org/10.7914/SN/Y5_2021

Schmandt, B., Jiang, C., & Farrell, J. (2019). Seismic perspectives from the western U.S. on magma reservoirs underlying large silicic calderas. *Journal of Volcanology and Geothermal Research*, *384*, 158–178. https://doi.org/10.1016/j.jvolgeores.2019.07.015

Shen, W., & Ritzwoller, M. H. (2016). Crustal and uppermost mantle structure beneath the United States. *Journal of Geophysical Research: Solid Earth*, *121*(6), 4306–4342. https://doi.org/10.1002/2016JB012887

Song, W., Schmandt, B., Wilgus, J., Lin, F.-C., Maguire, R., & Chaput, J. (2026). Silicic magma reservoir anisotropy persists through protracted crystallization and low strain rates. *Communications Earth & Environment*, *7*(1), 186. https://doi.org/10.1038/s43247-026-03214-7

Steck, L. K., Thurber, C. H., Fehler, M. C., Lutter, W. J., Roberts, P. M., Baldridge, W. S., et al. (1998). Crust and upper mantle P wave velocity structure beneath Valles Caldera, New Mexico: Results from the Jemez teleseismic tomography experiment. *Journal of Geophysical Research*, *103*(B10), 24301–24320. https://doi.org/10.1029/98JB00750

Terhemba, B. S., Yao, H., Luo, S., Gao, L., Zhang, H., & Li, J. (2022). P-wave velocity structure in the crust and the uppermost mantle of Chao Lake region of the Tan-Lu Fault inferred from teleseismic arrival time tomography. *Earthquake Science*, *35*(6), 427–447. https://doi.org/10.1016/j.eqs.2022.12.002

Tong, P. (2021). Adjoint-state traveltime tomography: Eikonal equation-based methods and application to the Anza Area in Southern California. *Journal of Geophysical Research: Solid Earth*, *126*(5), e2021JB021818. https://doi.org/10.1029/2021JB021818

Walker, J. D., Bowers, T. D., Black, R. A., Glazner, A. F., Farmer, G. L., & Carlson, R. W. (2006). A geochemical database for western North American volcanic and intrusive rocks (NAVDAT). In A. K. Sinha (Ed.), *Geoinformatics: Data to knowledge* (pp. 61–71). Geological Society of America. https://doi.org/10.1130/2006.2397(05

Wang, K., Tong, P., Zhang, Z., & Su, L. (2025). Mapping the crustal magmatic system and regional deformation of the Toba region by multi-parameter ambient noise adjoint tomography. *Journal of Geophysical Research: Solid Earth*, *130*(4), e2024JB030550. https://doi.org/10.1029/2024JB030550

Wang, K., Yang, Y., Jiang, C., Wang, Y., Tong, P., Liu, T., & Liu, Q. (2021). Adjoint tomography of ambient noise data and teleseismic P waves: Methodology and applications to Central California. *Journal of Geophysical Research: Solid Earth*, *126*(6), e2021JB021648. https://doi.org/10.1029/2021JB021648

Wessel, P., Luis, J. F., Uieda, L. a., Scharroo, R., Wobbe, F., Smith, W. H., & Tian, D. (2019). The generic mapping tools version 6. *Geochemistry, Geophysics, Geosystems*, *20*(11), 5556–5564. https://doi.org/10.1029/2019gc008515

Wilgus, J., Schmandt, B., Maguire, R., Jiang, C., & Chaput, J. (2023). Shear velocity evidence of upper crustal magma storage beneath Valles caldera. *Geophysical Research Letters*, *50*(5), e2022GL101520. https://doi.org/10.1029/2022gl101520

Wilks, M., Rawlinson, N., Kendall, J.-M., Nowacki, A., Biggs, J., Ayele, A., & Wookey, J. (2020). The coupled magmatic and hydrothermal systems of the restless Aluto caldera, Ethiopia. *Frontiers in Earth Science*, *8*, 579699. https://doi.org/10.3389/feart.2020.579699

Wu, S.-M., Huang, H.-H., Lin, F.-C., Farrell, J., & Schmandt, B. (2023). Extreme seismic anisotropy indicates shallow accumulation of magmatic sills beneath Yellowstone caldera. *Earth and Planetary Science Letters*, *616*, 118244. https://doi.org/10.1016/j.epsl.2023.118244

Xu, M., Wang, K., Chen, J., He, J., Liu, Q., Liu, Y., et al. (2025). Multilevel mechanisms driving intraplate volcanism in central Mongolia revealed by adjoint waveform tomography of receiver function and ambient noise data. *Earth and Planetary Science Letters*, *650*, 119137. https://doi.org/10.1016/j.epsl.2024.119137

Yao, S., Xu, T., Yang, T., Wu, C., Lin, J., Hua, Y., et al. (2025). Lithospheric structure of the central Altyn Tagh fault system tevealed by teleseismic travel-time tomography. *Seismological Research Letters*, *96*(4), 2300–2310. https://doi.org/10.1785/0220240314

Zhang, J., Dong, L., Liu, Y., Huang, C., Wang, Y., & Huilin, X. (2025). Eikonal equation-based elastic velocity reconstruction for multicomponent seismic reflection data. *Geophysics*, *90*(4), U47–U58. https://doi.org/10.1190/geo2024-0120.1

Zhou, X., Lan, H., Chen, L., Guo, G., Waheed, U. B., & Badal, J. (2023). A topography-dependent eikonal solver for accurate and efficient computation of traveltimes and their derivatives in 3D heterogeneous media. *Geophysics*, *88*(2), U17–U29. https://doi.org/10.1190/geo2021-0799.1